Photoionization spectroscopy of even-parity autoionizing Rydberg states of argon: Experimental and theoretical investigation of Fano profiles and resonance widths

J. D. Wright and T. J. Morgan
Department of Physics, Wesleyan University, Middletown, Connecticut 06459, USA

Leping Li, Quanli Gu, and J. L. Knee
Department of Chemistry, Wesleyan University, Middletown, Connecticut 06459, USA

I. D. Petrov and V. L. Sukhorukov
Rostov State University of Transport Communications, 344038 Rostov-on-Don, Russia

H. Hotop
Department of Physics, Kaiserslautern University of Technology, D-67653 Kaiserslautern, Germany

Using the $4s'[1/2]_0$ and $4s[3/2]_2$ metastable states of argon created in a plasma discharge we perform photoionization spectroscopy of even-parity autoionizing Ar(np') Rydberg states between the first and second ionization limits. Fitting the data to a sum of Fano-type or Shore-type profiles allows us to extract the widths and energies of the three overlapping resonance states $[1/2]_1$, $[3/2]_1$, and $[3/2]_2$ in the $11p'$ manifold. We compare the experimental analysis of the $11p'$ multiplet to theoretical calculations which are based on the configuration interaction Pauli-Fock approach with core polarization. Agreement between the experimental and theoretical resonance parameters is good.

PACS number(s): 32.30.−r, 32.70.−n, 31.15.V−

I. INTRODUCTION

Photoionization spectroscopy of the rare-gas atoms has a rich history of experiment and theory. The first observations of the autoionizing Rydberg states (ARS) in Ar, Kr, and Xe, located between the two lowest ionization thresholds $^2P_{3/2}$ and $^2P_{1/2}$ were made by Beutler [1]. These measurements led Fano [2–4] to discover his well-known formula (often addressed as Fano profile) describing the asymmetric line shapes of the resonances. The first analyses of experimental spectra using Fano profiles focused on single isolated resonances [2,3]. Shore presented alternative expressions for the description of autoionization resonances [5–7]. Later, isolated and overlapping ARS have been analyzed by multichannel quantum defect theory (MQDT) [8–12] as well as by relativistic MQDT involving *ab initio* parameters [13,14]. High resolution measurements of odd and even ARS $n\ell'[K]_J$ of the rare gas atoms Ne, Ar, Kr, and Xe have been performed by different experimental methods, including single vuv photon [15–18] or multiphoton excitation of the ground state [19–23] as well as one- or two-photon excitation of the metastable $(m+1)s'[1/2]_0$ and $(m+1)s[3/2]_2$ levels (m =2–5) of Ne-Xe (see, e.g., [23–32]).

The two main properties of the resonances which are derived from experimental spectra are the autoionization width Γ_n and the quantum defect μ_ℓ. The latter characterizes the resonance energy E_0 through its binding energy relative to the $mp^5_{1/2}$ ionization energy $I_{1/2}-E_0=hc\text{Ry}/(n-\mu_\ell)^2$ (hcRy =Rydberg energy for atom under consideration). The widths Γ_n depend strongly on the effective principal quantum number $n^* \equiv n-\mu_\ell$ and on ℓ', but also—for given $n\ell'$—on K =$\ell' \pm 1/2$ and the total angular momentum J. For a specified resonance series $n\ell'[K]_J$ the widths Γ_n are found to decrease

as n^{*-3} at sufficiently high n^* [13,15,17,25,26,30,33,34]; correspondingly, most of the members of a particular resonance series can be characterized by a single quantity, called reduced width Γ_r and defined by $\Gamma_r=n^{*3}\Gamma_n$ [15,17,25–34]. At lower n^* the reduced widths may vary somewhat with n^*, as recently discussed in some detail for the ARS in xenon [30].

Recently, rather comprehensive theoretical studies of the ARS of the heavier rare gas atoms have been carried out, elucidating the dependence of the reduced resonance widths and quantum defects on the quantum numbers ℓ', K, and J. In exploratory work involving the Pauli-Fock method, general trends were outlined [33] while in later papers the effects of electron correlation including core polarization were included and shown to be substantial in many cases [22,23,30,31,34]. In these papers references to other earlier experimental and theoretical work can be found. Very recently, the comparison of high resolution studies of the even Ne(np') resonances, accessed from the metastable Ne($3s'[1/2]_0, 3s[3/2]_2$) [31] as well as from the short-lived Ne($3s'[1/2]_1, 3s[3/2]_1$) levels [22], with configuration interaction Pauli-Fock with core polarization (CIPFCP) calculations demonstrated a strong influence of many-electron correlation effects on the spectral shapes and intensities. In particular, a strong interference between the direct $3s \rightarrow np$ and intershell $3s \rightarrow 3p \Rightarrow np$ pathways (the double arrow represents Coulomb interaction-induced mixing) for the transitions to the $2p^5np$ ARS with $J=0$ has been found [22]. Similarly, it was observed for the even np' resonances in Ar, Kr, and Xe [23,31] that the ARS were subject to substantial correlation effects, as documented by the great sensitivity of the resonance shapes to details of the interaction, resulting from the proximity of a Cooper-Seaton minimum in some of the channels. The existing experimental data for the Ar(np')

resonances, obtained by single uv photon excitation from the metastable levels [23,24,31,35–37], had insufficient optical resolution to fully resolve the overlapping line shapes.

In the present paper, we report well-resolved experimental measurements of the relative cross section for single photon ionization of the metastable $^{40}Ar(4s'[1/2]_0)$ and $^{40}Ar(4s[3/2]_2)$ atoms. Our work focuses on the energy region of the low-lying autoionizing $Ar(11p')$ resonances. The measured spectra, containing the two $11p'[1/2,3/2]_1$ and the three $11p'[1/2,3/2]_1, 11p'[3/2]_2$ overlapping resonances, respectively, are analyzed by using different analytical expressions, corresponding to sums of Fano-type [2,3] or Shore-type [5–7,23] profiles. We note that no hyperfine structure exists because the ^{40}Ar nucleus has zero spin. Determining accurate resonance parameters for each of the overlapping peaks in a multiplet presents a challenging problem. In order to solve this problem, we used a combination of theoretical calculations, experimental measurements, and analyses using nonlinear fitting.

The paper is organized as follows. In Sec. II, we describe the technique for computing the line shapes of the ARS taking into account many-electron correlations. We also use different expressions due to Fano and Cooper [2–4] and Shore [5–7] to analytically describe a spectrum with several adjacent resonances in terms of a small number of parameters which are determined from fits to experimental ARS spectra. In Sec. III, we present the experimental procedures for measuring the photoionization cross sections and describe the analysis of these spectra by means of Fano profiles and profile functions. In Sec. IV we compare the experimental results with those obtained by the CIPFCP calculations. In Sec. V, we conclude with a brief summary.

II. THEORY

A. General relations

The theory applied in the present paper for the computation of the line shapes is essentially the same as described elsewhere [23]. Therefore we dwell only on the important points. The $3p^5_{1/2}11p'[K]_J$ autoionizing resonances of argon can be accessed from the $3p^5_{1/2}4s'[1/2]_0$ and $3p^5_{3/2}4s[3/2]_2$ metastable states via the following transitions:

$$4s[3/2]_2 \overset{minor}{\to} 3p^5_{1/2}11p'([1/2]_1;[3/2]_{1,2}), \quad (1a)$$

$$4s'[1/2]_0 \overset{major}{\to} 3p^5_{1/2}11p'([1/2]_1;[3/2]_1). \quad (1b)$$

In the *major* transitions the total angular momentum of the core is conserved while it is decreased by one in the *minor* transitions. However, the oscillator strengths for both transitions are comparable because of a Cooper minimum in the *major* transitions and a strong influence of the many-electron correlations [23] on the *minor* transitions. In order to compute the photoionization cross sections we used the following scheme:

$$
3p^5 4s \qquad\qquad \to 3p^5(n/\varepsilon)\ell(\ell = p/f)
$$
$$
\Updownarrow \qquad\qquad\qquad \Updownarrow
$$
$$
\left\{ \begin{matrix} 3p^4\varepsilon\ell\{s/d\} & \text{(a)} \\ 3s^13p^6(n/\varepsilon)p & \text{(b)} \\ 3p^5\{s/d\} & \text{(c)} \end{matrix} \right\}
\left\{ \begin{matrix} 3p^44s\{s/d\} & \text{(d)} \\ 3s^13p^64s & \text{(e)} \\ 3p^5\{p/f\} & \text{(f)} \end{matrix} \right\}, \quad (2)
$$
$$
\quad\mathbf{ISCI}\qquad\qquad\quad\mathbf{FISCI}
$$

where the horizontal arrow denotes the electric dipole interaction and the vertical double-arrows denote the Coulomb interaction. A summation (integration) over all states contained in the braces was performed (continuum states were taken into account in a quasidiscrete manner). The basic configurations which contribute to the transition amplitude due to both initial state configuration interaction (ISCI) and final state configuration interaction (FISCI) are shown in scheme (2).

The photoionization cross section for the initial state $|i_0\rangle = |3p^54s[K_0]_{J_0}\rangle$ is

$$\sigma(\omega) = \sum_{\ell j J} \sigma_{\ell j J}(\omega). \quad (3)$$

For brevity, we omit the initial-state index i_0 in the notation of the total and partial cross sections, i.e., $\sigma(\omega) \equiv \sigma_{i_0}(\omega)$ and $\sigma_{\ell j J}(\omega) \equiv \sigma_{i_0\ell j J}(\omega)$. The partial cross sections are

$$\sigma_{\ell j J}(\omega) = \frac{4\pi^2\alpha a_0^2 \omega^{\pm 1}}{3(2J_0+1)} |\langle \overline{3p^5_{3/2}\varepsilon\ell_j J}\|\mathbf{D}\|i_0\rangle|^2, \quad (4)$$

where the signs (+) and (–) correspond to the length and velocity forms of the electric dipole operator **D**, respectively; ω denotes the exciting photon energy in atomic units; $\alpha = 1/137.036$ is the fine structure constant; atomic units are used in the matrix element; the square of the Bohr radius $a_0^2 = 28.0028$ Mb converts atomic units for cross sections to Mb $= 10^{-22}$ m^2; and the quantum numbers in the partial cross sections $\sigma_{\ell j J}(\omega)$ are self-explanatory. In the calculation of the reduced dipole matrix elements, entering Eq. (4), the correlations (2a)-(2e) are included via second order perturbation theory whereas the K-matrix technique was applied for inclusion of the correlation (2f).

The wave function of the final state $|\overline{3p^5_{3/2}\varepsilon\ell_j J}\rangle = |\overline{\beta E}\rangle$ entering Eq. (4) contains both nonresonant and resonant parts accounting for all the even-parity ARS via pathway (2f). This wave function was computed by applying the K-matrix technique [38] and the theory of interacting resonances in the complex calculus form [39] as

$$
|\overline{\beta E}\rangle = |\beta E\rangle + \sum_i \frac{\langle \overline{i^*}|\mathbf{H}^{ee}|\beta E\rangle}{E - E^{(i)}} \left[|\overline{i}\rangle \right.
$$
$$
\left. + \sum_{\beta'} \int dE' \frac{\langle \beta'E'|\mathbf{H}^{ee}|\overline{i}\rangle}{E - E' - \iota\delta} |\beta'E'\rangle \right], \quad (5)
$$

where summation over all resonances $|\overline{i}\rangle$ and integration (handled in a quasidiscrete manner) over all continua $|\beta'E'\rangle$ is performed. The total energy E entering Eq. (5) is connected with the photoelectron energy ε and the threshold

energy $I_{\beta E}$ via the usual relation: $E = I_{\beta E} + \varepsilon$. The "nonresonant" continuum wave functions $|\beta E\rangle$ were computed using the K-matrix technique [38]. The complex functions $|\bar{i}\rangle$ of the resonances are expressed via the real Pauli-Fock (PF) wave functions $|m\rangle$ of the discrete ARS:

$$|\bar{i}\rangle = \sum_m b_m^{(i)} |m\rangle. \qquad (6)$$

The complex energies of the resonances $E^{(i)}$ and their functions (6) were obtained as the solution of the secular equation with a complex symmetric (and therefore non-Hermitian) matrix:

$$\sum_m \left[(E^{(i)} - E_m)\delta_{mm'} - \langle m|\mathbf{H}^{ee}|m'\rangle \right.$$
$$\left. - \sum_\beta \int dE' \frac{\langle m|\mathbf{H}^{ee}|\beta E'\rangle\langle\beta E'|\mathbf{H}^{ee}|m'\rangle}{E - E' + \iota\delta} \right] b_m^{(i)} = 0, \quad (7)$$

where $b_m^{(i)}$ are complex numbers. The complex energy of each resonance determines its position E_i and width Γ_i via the relation

$$E^{(i)} = E_i - \frac{\iota}{2}\Gamma_i. \qquad (8)$$

The latter parameters determine the quantities, which only weakly depend on the principal quantum number n, i.e., the quantum defects μ and the reduced widths Γ_r via the following equations [17]:

$$E_i = I_{1/2} - hc\mathrm{Ry}/(n-\mu)^2, \qquad (9a)$$

$$\Gamma_r = \Gamma_i(n-\mu)^3, \qquad (9b)$$

where $I_{1/2}$ is the energy of the ionization threshold to which the ARS converge.

The function (6) allows one to compute the complex transition amplitude $D^{(i)}$ and Fano parameters, q_i and ρ_i^2 [2–4], for the resonance $|\bar{i}\rangle$ as

$$D^{(i)} = \left[\frac{4\pi^2\alpha a_0^2\omega^{\pm 1}}{3(2J_0+1)} \right]^{1/2} \left(\langle\bar{i}^*\|\mathbf{D}\|i_0\rangle \right.$$
$$\left. + \sum_\beta \int dE' \frac{\langle\bar{i}^*|\mathbf{H}^{ee}|\beta E'\rangle\langle\beta E'\|\mathbf{D}\|i_0\rangle}{E - E' + \iota\delta} \right), \quad (10a)$$

$$q_i = -\frac{\mathrm{Re}\, D^{(i)}}{\mathrm{Im}\, D^{(i)}}, \qquad (10b)$$

$$\rho_i^2 = \frac{2(\mathrm{Im}\, D^{(i)})^2}{\pi\Gamma_i\sigma_0}, \qquad (10c)$$

where the cross section σ_0 [4] is the nonresonant cross section computed by excluding the considered resonances in the range of interest (the tails from the adjacent resonances are included). For brevity, we omit the initial-state index i_0 in the notation of the complex transition amplitude, background,

and Fano parameters, i.e., $D^{(i)} \equiv D_{i_0}^{(i)}$, $\sigma_0 \equiv \sigma_{0_{i_0}}$, $q_i \equiv q_{i_0 i}$, and $\rho_i^2 \equiv \rho_{i_0 i}^2$.

B. Parametrization of the observed spectra

The photoionization cross section (3) can be represented by a formula due to Shore [see Eq. (3.33) in [7]] which is obtained as a solution of the problem "many resonances embedded in many continua" [5,6]:

$$\sigma(\omega) = C + \sum_i \frac{b_i + \epsilon_i a_i}{1 + \epsilon_i^2}. \qquad (11)$$

In this equation ϵ_i is the reduced energy, referred to the respective resonance energy and given by $\epsilon_i = 2(E - E_i)/\Gamma_i$. The parameter $C \equiv \sigma_0$ [4] denotes the nonresonant cross section that would be observed in the absence of a particular resonance group and is always positive. Equation (11) has been used by Ederer [40] to fit profiles of partially overlapping resonances in Kr and Xe. The terms of the sum in Eq. (11) are addressed as "profile functions $P_i(\epsilon_i)$"; they can be expressed via the Fano parameters, q_i, and ρ_i^2 [2,3] [see also Eqs. (10b) and (10c)] as follows:

$$P_i(\epsilon_i) = \frac{b_i + \epsilon_i a_i}{1 + \epsilon_i^2} = \sigma_0\rho_i^2\left[\frac{(q_i + \epsilon_i)^2}{1 + \epsilon_i^2} - 1 \right] \qquad (12)$$

with the evident connection between the parameters q_i, ρ_i^2 and b_i, a_i:

$$a_i = 2q_i\sigma_0\rho_i^2, \qquad (13a)$$

$$b_i = \sigma_0\rho_i^2(q_i^2 - 1). \qquad (13b)$$

The profile function for the case of one resonance-many continua was introduced by Fano and Cooper in the form of the right-hand side of Eq. (12) [see Eq. (8.5) in [4]]. Equation (11) can be written in terms of these profile functions as

$$\sigma(\omega) = \sigma_0 + \sum_i \sigma_0\rho_i^2\left[\frac{(q_i + \epsilon_i)^2}{1 + \epsilon_i^2} - 1 \right] \qquad (14)$$

and was recently used for the parametrization of *ab initio* computed line shapes by e.g., Petrov *et al.* [23,41]. The parameter σ_0 includes the tails of adjacent resonances and from the calculational point of view is obtained when the parametrized resonance(s) are simply removed from the range of interest. The shape parameter (or profile index) q_i in Eq. (14) has the same meaning as that introduced in [2,3]. In the "many resonance—many continua" case, the parameter ρ_i^2, however, no longer has such a clear meaning as in the "one resonance-many continua" case considered by Fano [3]. In contrast to the latter case, ρ_i^2 in Eq. (14) can even be larger than unity.

Note that the profile functions $P_i(\epsilon_i)$ can assume both positive and negative values; the maximum h_i at $\epsilon_i = 1/q_i$ is positive $[h_i = P_i(1/q_i) = \sigma_0\rho_i^2 q_i^2]$ while the minimum d_i at $\epsilon_i = -q_i$ is negative $[d_i = P_i(-q_i) = -\sigma_0\rho_i^2]$ [6]. We find it useful to introduce the dimensionless "resonance contrast" by

$$\eta_i^2 \equiv (h_i - d_i)/\sigma_0 = \rho_i^2(q_i^2 + 1). \tag{15}$$

Graphically, σ_0 is the background level underlying the profile functions. The profile function $P_i(\epsilon_i)$ has a peak of finite height h_i and a trough of finite depth $|d_i|$, one but not both of which can be zero depending on the characteristic ratio, $q_i^2 = h_i/|d_i|$. In graphical terms, the parameter η_i^2 is the dimensionless trough-to-peak height, i.e., the height, measured from the bottom of the trough to the top of the peak of profile function $P_i(\epsilon_i)$, expressed as a fraction of σ_0. The parameter ρ_i^2 is the dimensionless trough depth, i.e., the trough depth of profile function $P_i(\epsilon_i)$ expressed as a fraction of σ_0. We also consider the parameter σ_{ai}, which is equivalent to the trough depth, and the parameter σ_b', which is the baseline level for a cross section composed of Fano-type profiles as shown in the next paragraph.

Using the appropriate relationships $\sigma_0 = \sigma_b' + \Sigma_i \sigma_{ai}$ and $\rho_i^2 = \sigma_{ai}/(\sigma_b' + \Sigma_i \sigma_{ai})$ Eq. (14) can be rewritten as [see Eq. (5.1) from [7]]

$$\sigma(\omega) = \sigma_b' + \sum_i \sigma_{ai} \frac{(q_i + \epsilon_i)^2}{1 + \epsilon_i^2}. \tag{16}$$

In this equation $\sigma_{ai} = \sigma_0 \rho_i^2$; the constant contribution $\sigma_b' = \sigma_0(1 - \Sigma_i \rho_i^2)$ can be negative, while the background cross section σ_0 in Eq. (14) is always positive. We note that formulas structured as Eq. (16) have often been used in order to fit multicomponent autoionization spectra with superpositions of independent Fano profiles $F_i(\epsilon_i)$,

$$F_i(\epsilon_i) = \sigma_{ai} \frac{(q_i + \epsilon_i)^2}{1 + \epsilon_i^2}, \tag{17}$$

using the restriction $\sigma_b' \geq 0$. By imposing this restriction part of the physics of the problem may be missed.

C. Results of calculations

In computing the photoionization cross sections in the energy range of the $11p'[K]_J$ multiplet we used the configuration interaction Pauli-Fock approximation with core polarization (CIPFCP) [42,43] applying scheme (2). The parameters for computing the effective value of the Coulomb interaction entering scheme (2) and the core polarization potential were the same as in [23]. The results of the calculations are shown in Figs. 1 and 2. The partial cross sections $\sigma_{\ell jJ}$ given by Eq. (4) and the subtotal cross sections given by Eq. (18) are shown in the two upper panels of Fig. 1 (for the initial $4s[3/2]_2$ level) and in the upper panel of Fig. 2 (for the initial $4s'[1/2]_0$ level).

$$\sigma_J(\omega) = \sum_{\ell j} \sigma_{\ell jJ}(\omega). \tag{18}$$

The $4s[3/2]_2 \rightarrow 11p'[K]_1$ transitions are strongly dominated by the $3p^5\epsilon p_j$ channels [see Fig. 1(a)] whereas for the transitions $4s[3/2]_2 \rightarrow 11p'[K]_2$ and $4s'[1/2]_0 \rightarrow 11p'[K]_1$ the channels $3p^5\epsilon f_j$ also contribute, albeit at a low level [see Figs. 1(b) and 2(a), respectively]. The contributions from the $11p'[3/2]_1$ and $11p'[1/2]_1$ resonances interfere with different signs in the channels $4s[3/2]_2 \rightarrow 3p^5\epsilon p_{1/2;1}$ and
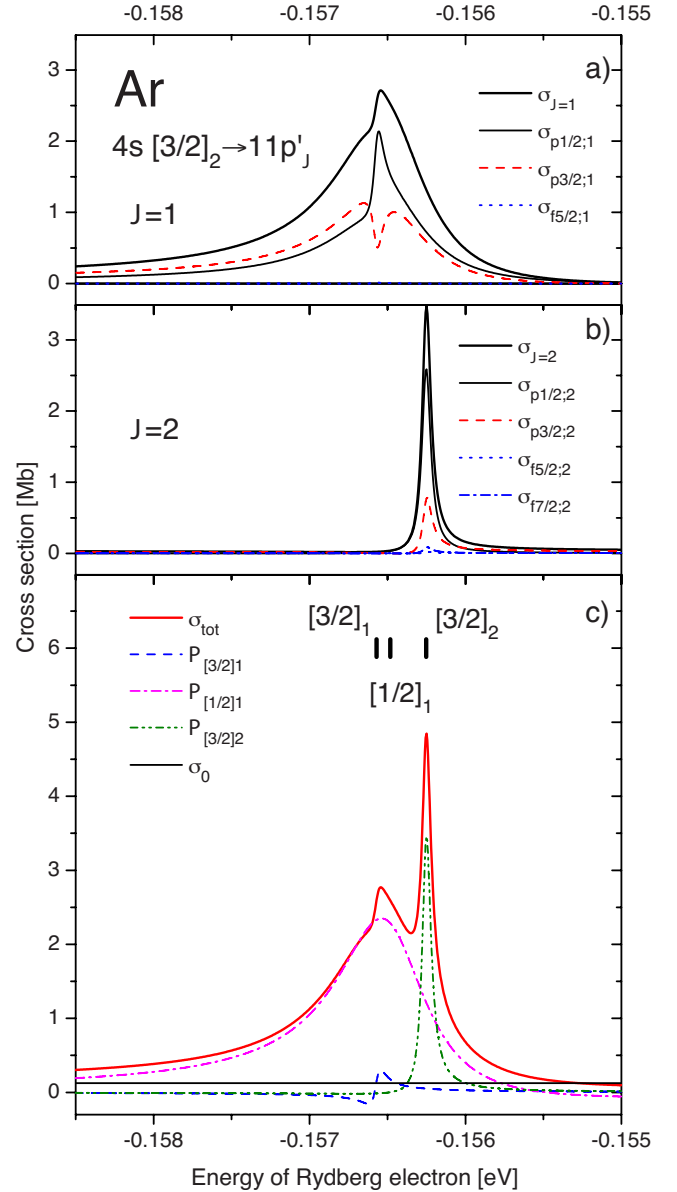

FIG. 1. (Color online) Partial and total cross sections for the transition $4s[3/2]_2 \rightarrow 11p'[K]_J$ computed with the CIPFCP approach. The theoretical profile functions $P_{[K]_J}(\omega)$ (12) are shown in the bottom panel.

$4s[3/2]_2 \rightarrow 3p^5\epsilon p_{3/2;1}$ (cf. cross sections $\sigma_{p1/2;1}$ and $\sigma_{p3/2;1}$); this effect could be revealed by a future experimental study of the photoelectron angular distribution.

In the bottom panels of Figs. 1 and 2 we show the respective resonance contributions $P_i(\epsilon_i)$, the background cross section σ_0, and the total cross section for photoionization of the $J_0 = 2$ and $J_0 = 0$ metastable levels in the energy range of the $11p'$ resonances. This representation of the cross sections by profile functions (including the background term σ_0) offers a different composition of the total cross section by means of resonance-specific $[K]_J$ channels as compared to the more detailed, final-channel specific description shown in the upper panels in Figs. 1 and 2. The total cross sections are of course the same in both descriptions.
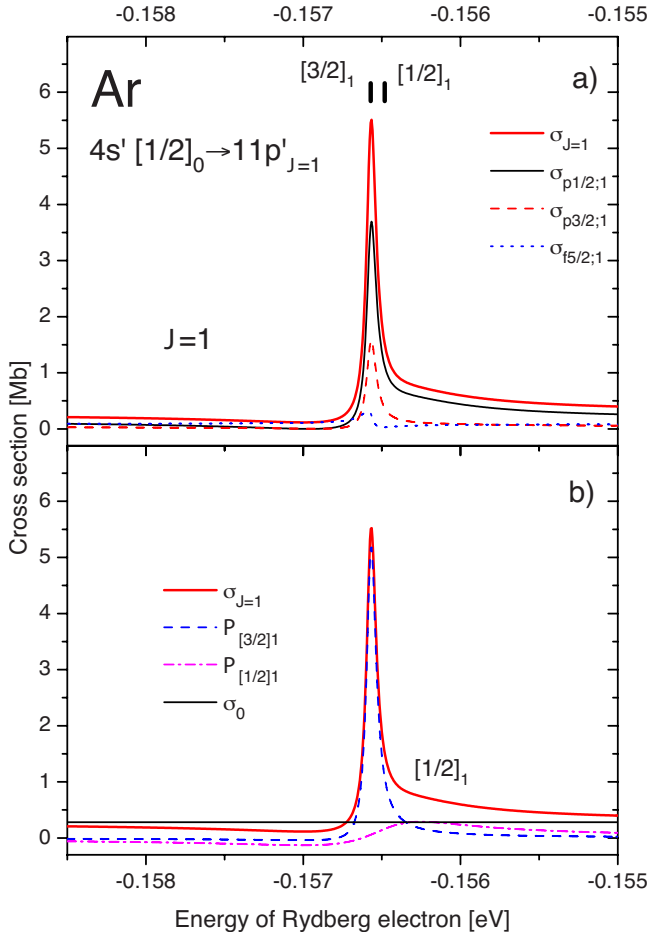
FIG. 2. (Color online) Partial and total cross sections for the transition $4s'[1/2]_0 \rightarrow 11p'[K]_1$ computed with the CIPFCP approach. The theoretical profile functions $P_{[K]_J}(\omega)$ (12) are shown in the bottom panel.

FIG. 3. Diagram for excitation of atomic argon from the ground state via a metastable state to autoionizing Rydberg states.

The results of this calculation are depicted in Figs. 1(c) and 2(b) for the $4s[3/2]_2 \rightarrow 11p'$ and $4s'[1/2]_0 \rightarrow 11p'$ transitions, respectively. One can recognize from Figs. 1 and 2 that the partial cross sections described by Eq. (4) cannot be represented via the profile functions [cf. Figs. 1(a) and 1(c)] whereas the total cross sections are identical. The $11p'[3/2]_1$ resonance has a rather different appearance when excited from either metastable level. The $4s[3/2]_2 \rightarrow 11p'[3/2]_1$ transition exhibits a dispersion-type low-intensity profile while the $4s'[1/2]_0 \rightarrow 11p'[3/2]_1$ transition is a dominant, nearly symmetric peak. Therefore the parameters of this resonance can be determined more precisely from the analysis of the $4s'[1/2]_0 \rightarrow 11p'[3/2]_1$ transition. Parameters of the broad $11p'[1/2]_1$ resonance can be determined more precisely from the analysis of the $4s[3/2]_2 \rightarrow 11p'[3/2]_1$ transition whereas the $4s'[1/2]_0 \rightarrow 11p'[3/2]_1$ transition provides a rather weak contribution, exhibiting a dispersion-type profile which produces a tail in the overall resonance structure toward higher energies.

III. EXPERIMENT

The energy diagram corresponding to our experiment and scheme (1a) and (1b) is depicted in Fig. 3. A KDP crystal
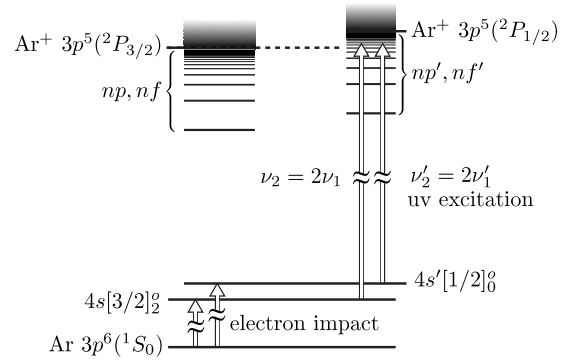
frequency-doubles the visible light output of a Lumonics dye laser pumped at 532 nm by the second harmonic of a pulsed Continuum Nd:YAG laser to produce tunable uv radiation (denoted as ν_2 and ν_2' in Fig. 3) with a bandwidth of 0.22 cm^{-1} over the range of 33 250–35 420 cm^{-1} using Rhodamine 610 and 590 laser dyes (frequencies ν_2' and ν_2). Light in this wave-number range efficiently excites argon atoms to autoionizing Rydberg states just above the first ionization limit from either the $4s'[1/2]_0$ (94 553.671 cm^{-1}) or $4s[3/2]_2$ (93 143.766 cm^{-1}) metastable state [44,45]. We use the values of 33 966.076(3) cm^{-1} for the first, Ar$^+$($^2P_{3/2}$), ionization limit and 35 397.659(4) cm^{-1} for the second, Ar$^+$($^2P_{1/2}$), ionization limit relative to the $4s[3/2]_2$ metastable state (the ground state ionization energies are 127 109.842(4) and 128 541.425(4) cm^{-1}, respectively [28,44,45]). The $4s'[1/2]_0$ and $4s[3/2]_2$ metastable states are populated via electron impact in a plasma discharge using a supersonic beam. The relative energy scale of the experimental spectra was established by frequency markers from an etalon (free spectral range 0.70 cm^{-1}) and has an estimated uncertainty of ± 0.06 cm^{-1} over a range of 25 cm^{-1}. The *absolute* energy scale could not be accurately established; therefore the Rydberg binding energy of the sharpest resonance in the $4s[3/2]_2 \rightarrow 11p'$ spectrum, namely $11p'[3/2]_2$, was adjusted to the theoretical value. In the $4s'[1/2]_0 \rightarrow 11p'$ spectrum the binding energy of the $[3/2]_1$ resonance was adjusted to that obtained in the $4s[3/2]_2 \rightarrow 11p'$ spectrum, see Table I.

The experimental value of σ_0 cannot be absolutely determined for either of the measured photoionization spectra because neither cross section scale is calibrated. However, the relative scale is accurate so that the dimensionless resonance contrast (η^2) and dimensionless trough depth (ρ^2) of each resonance can be determined. The experimental values of σ_0 are adjusted to match those of theory so that each experimental value of σ_b' can be compared with that of theory, see Table I. Analysis of a time-of-flight channel that contained no signal allowed for the purely electronic background value to be determined and subtracted from the data to obtain a properly zeroed photoionization signal. In addition, we were careful to avoid the effects of detector saturation.

A schematic diagram of the experimental apparatus can be found in Fig. 4. The supersonic beam emerges from a pulsed nozzle into the discharge region, continues through an ion-

TABLE I. Computed and measured parameters for the line profiles in transitions (1a) and (1b).

		$4s'[1/2]_0 \rightarrow 11p'[K]_1$		$4s[3/2]_2 \rightarrow 11p'[K]_J$		
		$[1/2]_1$	$[3/2]_1$	$[1/2]_1$	$[3/2]_1$	$[3/2]_2$
Theory		$\sigma_0=0.282$ Mb		$\sigma_0=0.1262$ Mb		
		$\sigma_b'=0.114$ Mb		$\sigma_b'=-0.112$ Mb		
	μ	1.6754	1.6781	1.6754	1.6781	1.6686
	$\Gamma_r(\mathrm{cm}^{-1})$	**4479**[a]	481	**4479**	481	**447**
	q	1.5	11.6	−6.0	1.4	14.1
	ρ^2	0.457	0.137	0.512	1.236	0.138
	η^{2} [b]	1.49	18.57	18.94	3.66	27.57
Experiment		$\sigma_0= 0.282$ Mb		$\sigma_0= 0.1262$ Mb		
Model I[c]		$\sigma_b'=0$ Mb		$\sigma_b'=0$ Mb		
	μ	1.6755	*1.6773*	1.6755	1.6773	*1.6686*
	$\Gamma_r(\mathrm{cm}^{-1})$	3584	636	3584	636	295
	q	>100	2.9	−8.8	2.7	17.7
	η^2	1.2	14.3	13.7	6.0	24.0
Model II[d]		$\sigma_b'=0.05(0.07)$ Mb		$\sigma_b'=-0.7(0.6)$ Mb		
	μ	1.6762(9)	*1.6790*	1.6762(9)	1.6790(9)	*1.6686*
	$\Gamma_r(\mathrm{cm}^{-1})$	3015(1100)	533(40)	3015(1100)	533(40)	321(110)
	q	5(3)	4(8)	−10(4)	0. 4(1.0)	11(4)
	η^2	2(1)	15(8)	17(2)	7(4)	24(4)
Model III[e]		$\sigma_b'=0.07$ Mb		$\sigma_b'=-0.8$ Mb		
	μ	1.6762	*1.6792*	1.6762	1.6792	*1.6686*[f]
	$\Gamma_r(\mathrm{cm}^{-1})$	2931	535	2930	535	324
	q	4.6	4.7	−10.8	0.3	11.1
	η^2	2	15	18	7	24

[a]Values lying out of the experimentally estimated confidence interval are shown in bold.

[b]Resonance contrast $\eta_i^2=\rho_i^2(q_i^2+1)$ [see Eq. (15)].

[c]Constraints (19) and (20) are used; background is restricted, i.e., $\sigma_b'\geq 0$.

[d]Constraints (19) and (20) are used; statistical error bars are shown in parenthesis.

[e]Constraints (19) and (20) are used; background is unrestricted, i.e., σ_b' can be negative.

[f]Values adjusted to match that of theory are shown in italics.

sweeper electric field, and passes through a skimmer into a second differentially pumped vacuum chamber with a residual pressure of approximately 5×10^{-7} torr. The second vacuum chamber houses a conventional time-of-flight mass spectrometer [46] which uses pulsed electric fields, ion optics, and microchannel plates to extract, focus, and detect the Ar^+ ions produced by photoionization. Each laser excited pulse of ions strikes the detector over a mass specific range of times. The detector then produces an amplified pulse
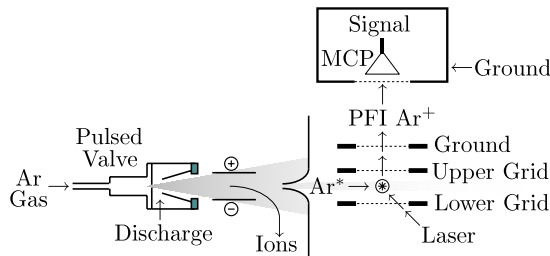

FIG. 4. (Color online) Schematic diagram of the experimental apparatus.

which feeds into a digital oscilloscope. The oscilloscope records the pulse in time-ordered channels with nanosecond time resolution. The signal in each channel is recorded as a function of the laser wave number. The spectrum as a function of wave number does change slightly depending on which signal channel is plotted. It was decided that integrating the signal over all channels spanning the pulse created by argon ions at each wave number in a laser scan would give the most accurate representation of the photoionization cross section. The photoionization occurs between two parallel plates of the ion-optic assembly in a small volume determined by the focused uv laser light (diameter 0.36 mm). Typical uv intensities amounted to 10 $\mathrm{MW/cm}^2$.

A. Experimental data

Visual inspection of the experimental data in Figs. 5(a) and 5(b) indicates that for excitation from the initial $4s[3/2]_2$ metastable level all three transitions (1a) make a perceptible contribution to the measured spectrum. However, the three transitions significantly overlap.
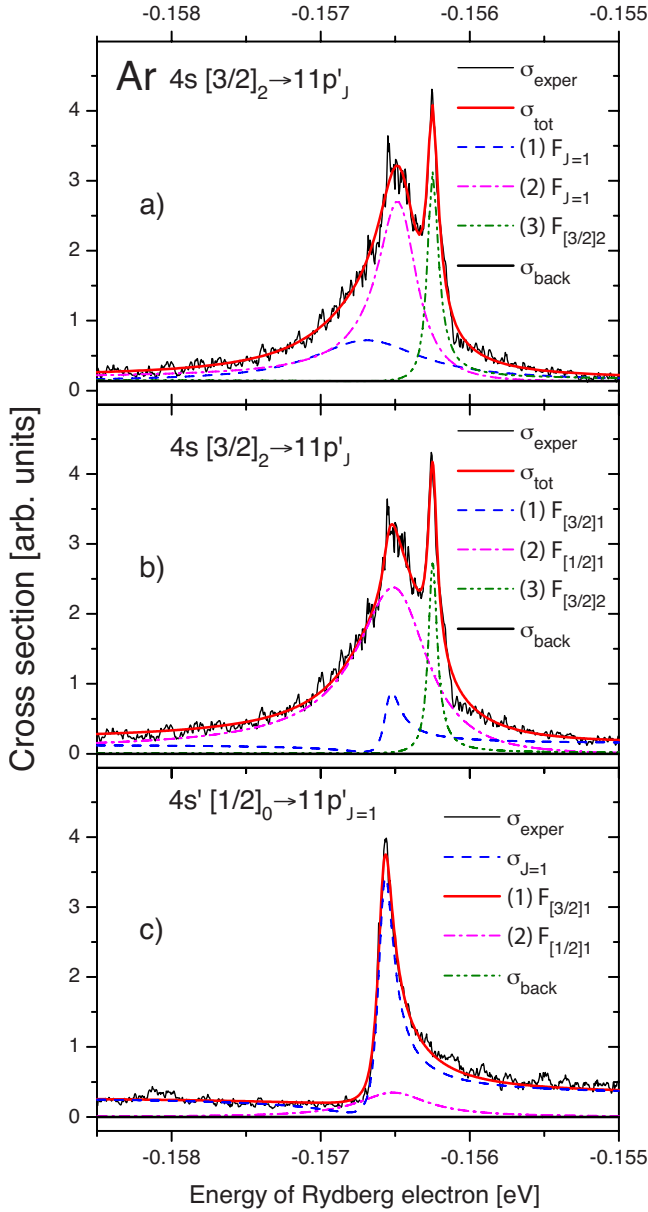
FIG. 5. (Color online) Photoionization cross section for the (a) and (b) $4s[3/2]_2 \rightarrow 11p'[K]_{J=1,2}$ and (c) $4s'[1/2]_0 \rightarrow 11p'[K]_{J=1}$ transitions analyzed for Fano-type model I. For the spectra shown in panels (b) and (c) constraints (19) and (20) were used. No constraints were used for the spectrum shown in panel (a).

In order to gain more information about the $11p'$ multiplet, the two $J=1$ resonance states were also excited from the $4s'[1/2]_0$ metastable level according to scheme (1b), using uv light over the range of $32\,710-34\,740$ cm^{-1}. Figure 5(c) shows the measured photoionization spectrum of the $4s'[1/2]_0 \rightarrow 11p'$ multiplet. The spectrum shows at least one transition. The resonance shows an asymmetry on its high energy side. This asymmetry indicates the possibility of a Fano line shape involving a single resonance or a contribution from another dipole-allowed transition or a combination of both effects. It is clear that the components of this spectrum have quite a different appearance when excited from the other metastable state [see Figs. 5(a) and 5(b)].

Both of the metastable states live many orders of magnitude longer than the autoionizing Rydberg states. Thus the spectral width of the transitions is determined by the natural width of the ARS. However, the laser and other instrumental factors can artificially broaden the transitions.

The effects of saturation broadening on the observed widths of the $11p'$ resonances are estimated to be 10% or less based on an examination of the $9f'[5/2]_3$ resonance (whose width was accurately determined in a previous high-resolution study [23]) and on the calculated peak cross sections for the $11p'$ (≤ 5 Mb) and $9f'$ (20 Mb) resonances. Residual electric fields in the interaction region, due to the presence of nondissipated charges during the time between the high voltage extraction pulses and/or bombardment of the extraction grid with charged particles from the discharge, are less than 1 V/cm, and usually smaller than this, based on the observed shift in the Rydberg series convergence limit. Doppler broadening is estimated to be less than 0.005 cm^{-1} at a central wave number of 34 000 cm^{-1} based on the beam velocity, ~ 550 m/s, and apparatus geometry.

These sources of artificial broadening and the laser linewidth can be factored into an analysis of the measured spectra and the natural width of the autoionizing Rydberg states can be extracted by fitting the data. The overlapping nature of the resonances necessitates a multipeak fit. In order to perform such a multipeak fit we use the procedure described in the next section.

B. Analysis procedure

In the course of this work we used three different fitting models.

Model I. Fano-type model using Eq. (16) with profile functions $F_i(\epsilon_i)$ (17) which are always positive and also restricting the σ_b' background cross section to *positive* values. In the first trial fits the two spectra were fitted independently, i.e., the width and energies of the $11p'[1/2]_1$ and $11p'[3/2]_1$ resonances as they appear in transitions (1a) and (1b) are considered as independent quantities. At a later stage we introduced the constraints

$$\Gamma_{[1/2]_1} = \Gamma'_{[1/2]_1},$$

$$\Gamma_{[3/2]_1} = \Gamma'_{[3/2]_1}, \tag{19}$$

and

$$E_{[1/2]_1} - E_{[3/2]_1} = E'_{[1/2]_1} - E'_{[3/2]_1}, \tag{20}$$

where the primed values refer to those for the spectrum excited from $4s'[1/2]_0$.

Model II. Shore-type model using Eq. (14) with the profile functions $P_i(\epsilon)$ given by Eq. (12) which are negative in one of the wings and with the background σ_0 which is always positive. Constraints (19) and (20) were imposed.

Model III. Modified Fano-type model using Eq. (16) and allowing for the possibility of a *negative* σ_b' background cross section. Constraints (19) and (20) were imposed.

For each model, the calculated profiles were convoluted with an instrumental profile. The instrumental profile was

consistent with a Lorentzian of 0.22 cm^{-1} full width at half maximum.

The fitting procedure consisted of the following steps.

(1) Graphically estimate the parameters for each model and calculate a preliminary fit to the multiplet. It is often helpful to estimate the trough depth $|d_i|$, peak height h_i, full width at half-maximum amplitude $\Gamma_i^{[\mathrm{FWHM}]}$, and energy position at maximum amplitude $E_i^{[\mathrm{M}]}$ for each resonance. Here, maximum amplitude refers to the peak height or trough depth, whichever is greater. These quantities give

$$\sigma_{ai} = |d_i|, \tag{21}$$

$$q_i = \pm \sqrt{h_i/\sigma_{ai}}, \tag{22}$$

$$\Gamma_i = \Gamma_i^{[\mathrm{FWHM}]}\sqrt{|q_i|^{1+t_i}/(q_i^2 + |q_i|^{1-t_i} + 1)}, \tag{23}$$

$$E_i = E_i^{[\mathrm{M}]} - \frac{1}{2}\Gamma_i(t_i q_i)^{-t_i}, \tag{24}$$

$$P_i(\epsilon_i) = \sigma_{ai}\left[\frac{(q_i + \epsilon_i)^2}{1 + \epsilon_i^2} - 1\right], \tag{25}$$

and the Fano profile $F_i(\epsilon_i)$. The sign of q_i is positive when the trough occurs on the low-energy side of the peak. The variable t_i characterizes the "type" of profile which is "positive" ($t_i = +1$) when the peak height is greater than the trough depth ($h_i > \sigma_{ai}$), "neutral" ($t_i = 0$) when $h_i = \sigma_{ai}$, and "negative" ($t_i = -1$) when $h_i < \sigma_{ai}$. One can estimate σ_0 by extrapolating the signal level far from all resonances and calculate

$$\sigma_b' = \sigma_0 - \sum_i \sigma_{ai}, \tag{26}$$

$$\rho_i^2 = \sigma_{ai}/\sigma_0. \tag{27}$$

(2) Use the estimated parameters obtained in step (1) to calculate the initial fit and graphically compare it with the experimental data. Manually adjust any one of the parameters, recalculate the fit, and observe the change. Iterate this process using trial and error to improve the fit and obtain reasonable estimates for all quantities in the parameter set.

(3) Start with the set of parameters obtained in steps (1) and (2) and vary them to minimize the residual errors between the fit and the data using the Levenberg-Marquardt algorithm [47]. If the algorithm converges then one obtains a set of optimized parameters. Using these parameters, one can recalculate the fit function omitting the step of convolution with the laser profile. Through this process of deconvolution, one obtains a function that best fits the natural spectrum of the atom.

In the following section we first describe fits obtained with model I. Then we discuss in detail the fits with model II which we consider physically most appropriate. Finally we show fits obtained with model III which will be observed to yield essentially the same resonance parameters and a substantial *negative* background.

IV. DISCUSSION OF THE EXPERIMENTAL SPECTRA AND COMPARISON WITH THEORY

The two fits to the experimental data in Figs. 5(a) and 5(b) demonstrate that a statistically equivalent description of the measured spectrum excited from the $4s[3/2]_2$ level can be obtained with very different sets of the resonance parameters. The fit in Fig. 5(a) basically represents the sum of three near Lorentzian peaks (1), (2), and (3) with q parameters of about +70, −10, and +11 and reduced widths of 5634, 1921, and 404 cm^{-1}, respectively. Peak (3) is identified with the $11p'[3/2]_2$ resonance because of its absence in Fig. 5(c). The resonance energies of peak (1) and (2) relative to that of peak (3) are −3.58 and −1.74 cm^{-1}. In contrast, the fit in Fig. 5(b) yields q parameters of about +2.6, −8.6, and +21, reduced widths of 636, 3584, and 295 cm^{-1}, respectively, and energy separations of −2.39 and −1.85 cm^{-1}. In comparison with the theoretical prediction only the fit result in Fig. 5(b) appears to be realistic. This is confirmed by fits to the spectrum excited from the $4s'[1/2]_0$ level in Fig. 5(c). It cannot be described by a combination of two peaks with the same widths of those for the peaks (1) and (2) in Fig. 5(a). Using the width of the corresponding two peaks in Fig. 5(b), however, a satisfactory fit of this spectrum is obtained. The two fits in Figs. 5(b) and 5(c) allow us—with reference to the theoretical prediction—to identify the narrow asymmetric resonance at the lowest energy, peak (1), as $11p'[3/2]_1$ and the broadest resonance, peak (2), as $11p'[1/2]_1$ [see also Fig. 1(c)].

Implementation of the physical constraints (19) and (20) in fits with model II eliminates many possibilities for the initial estimates. Even then the results of the fitting procedure still depended on the initial estimates for the parameter set. Thus it was helpful to use starting parameters close to the theoretically predicted values. The resulting set of converged parameters is documented in Table I (model II). The spectra obtained using model II and the respective profile functions are depicted in Figs. 6(a) and 7(a). Note that the cross-section scale in the experimental data was adjusted to that of the computed spectra. The residuals of the fitting procedure are shown in Figs. 6(b) and 7(b). Figures 6(c) and 7(c) represent the computed profiles of Figs. 1(a) and 2(a) convoluted with the instrumental profile. Comparison between the measured [Figs. 6(a) and 7(a)] and computed [Figs. 6(c) and 7(c)] total cross sections exhibits reasonable accord between experiment and theory.

A main result of the model II fits is the explanation of the rather sharp feature located close to the binding energy −0.1566 eV in Fig. 6(a) for excitation from $4s[3/2]_2$: it is caused by the superposition of the broad peaklike positive profile ($q = -10$) due to $11p'[1/2]_1$ and a windowlike negative profile ($q = 0.4$) due to $11p'[3/2]_1$. The fitted (reduced) width of the $11p'[1/2]_1$ resonance (3015 cm^{-1}) is 33% smaller than the computed value (4479 cm^{-1}) while the fitted (reduced) width of the $11p'[3/2]_1$ resonance (533 cm^{-1}) is 11% larger than the computed value (481 cm^{-1}). The contribution of the $11p'[3/2]_2$ resonance is a sharp peaklike feature ($q = 11$) whose fitted (reduced) width (321 cm^{-1}) is 28% lower than the calculated result (447 cm^{-1}). The fitted shape parameters q as well as the contrast values η^2 are in
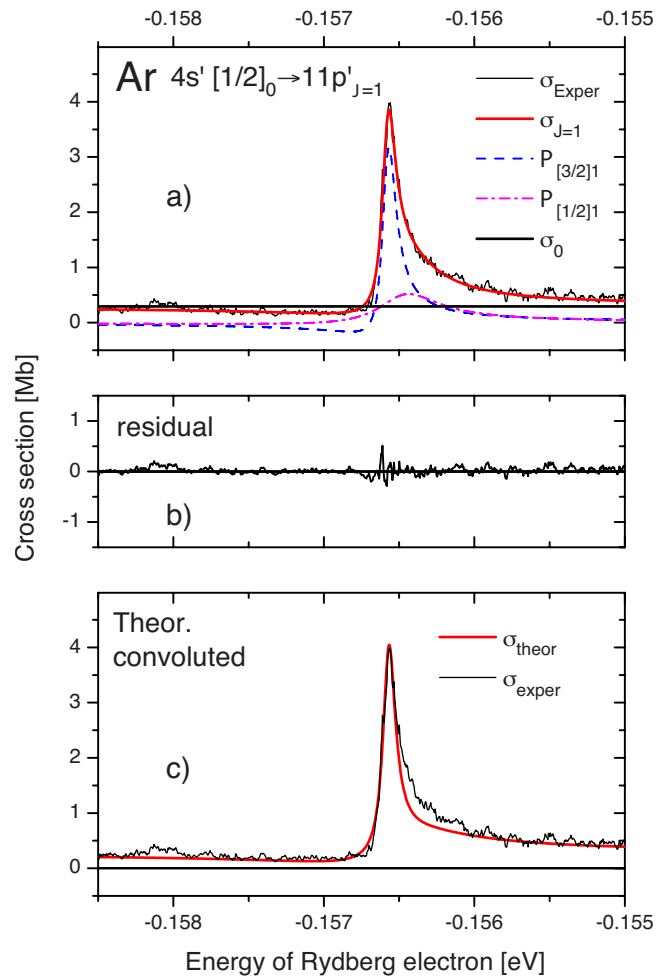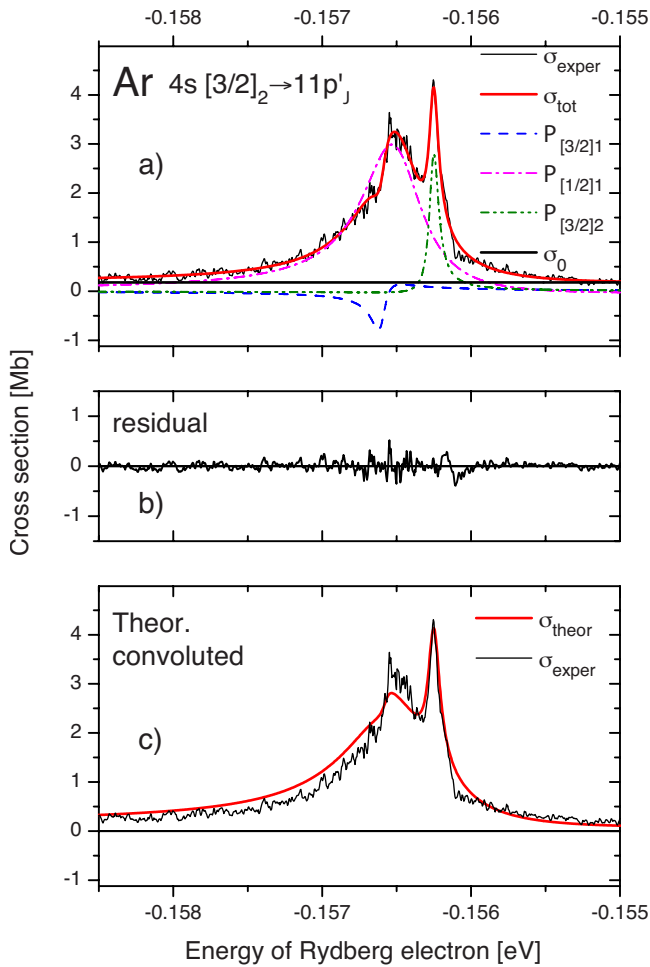
FIG. 6. (Color online) Photoionization cross section for the $4s[3/2]_2 \rightarrow 11p'[K]_{J=1,2}$ transitions. Graph (a) shows the experimental data and fit to the sum of three profile functions (model II). Graph (b) shows the residual errors of the fit. Graph (c) compares the measured and computed profiles. Theoretical profile is convoluted with a Lorentzian (FWHM=0.22 cm^{-1}) simulating the laser profile.

FIG. 7. (Color online) Photoionization cross section for the $4s'[1/2]_0 \rightarrow 11p'[K]_{J=1}$ transitions. Graph (a) shows the experimental data and fit to the sum of three profile functions (model II). Graph (c) compares the measured and computed profiles. Theoretical profile is convoluted with a Lorentzian (FWHM=0.22 cm^{-1}) simulating the laser profile.

satisfactory overall agreement with those calculated.

The $11p'$ spectrum excited from the $4s'[1/2]_0$ level [Fig. 7(a)] is well-described by the superposition of the dominant somewhat asymmetric $11p'[3/2]_1$ ($q=4$) contribution and the weaker asymmetric $11p'[1/2]_1$ profile ($q=5$). The main difference between experiment and theory is in the tail at higher energies which is broader in the measured data. Note that the energy scale of this spectrum was fixed with reference to the position of the $11p'[3/2]_1$ resonance, as calculated with the quantum defect obtained in the fit of the experimental spectrum in Fig. 6(a); the energy spacing between the $11p'[3/2]_1$ and $11p'[1/2]_1$ resonances was fixed to the fitted value of Fig. 6(a).

Good overall agreement between the computed parameters and the parameters from the model II fits is observed, especially for the most intense resonances (large η^2 parameter in Table I). The agreement between the computed and the fitted profile parameters for the $4s[3/2]_2 \rightarrow 11p'$ transition is better than for the transition $4s'[1/2]_0 \rightarrow 11p'$. Possibly this has to do with the presence of a nearby Cooper minimum in the *major* $4s'[1/2]_0 \rightarrow 11p'$ transition which results in a substantial sensitivity of the computed resonance parameters for this transition to the exact position of this minimum [23]. In contrast, the "correlational" *minor* $4s[3/2]_2 \rightarrow 11p'$ transition does not possess a nearby Cooper minimum [23].

In Figs. 8(a) and 8(b), we compare the experimental spectra with the fits obtained with model III. Since models II and III are mathematically equivalent it is not surprising that the fitted width and shape parameters q obtained with model III are in close agreement with those of model II (see Table I). Note that a substantial *negative* background is needed in order to describe the spectrum excited from the $4s[3/2]_2$ level with model III. This requirement is a consequence of the mathematical equivalence of the fits with models II and III. Fits with model I (in which a negative background is ruled out, see Fig. 5) yield profile parameters, notably for the $4s[3/2]_2 \rightarrow 11p'[3/2]_1$ resonance and for the broad $4s'[1/2]_0 \rightarrow 11p'[1/2]_1$ resonance, which differ rather strongly from those obtained with models II and III. We take
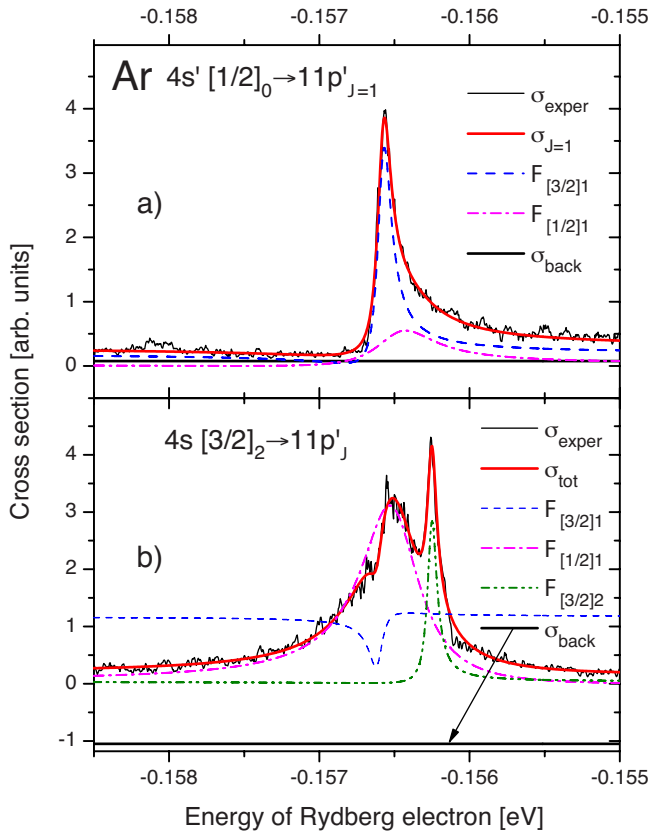
FIG. 8. (Color online) Photoionization cross section for the (a) $4s'[1/2]_0 \rightarrow 11p'[K]_{J=1}$ and (b) $4s[3/2]_2 \rightarrow 11p'[K]_{J=1,2}$ transitions analyzed with Fano-type model III.

this as evidence for a failure of model I-type fits to yield a proper description of the Ar(11p') autoionization spectra, excited from the two metastable Ar levels. Furthermore, the theoretically calculated values of ρ_i^2 and σ_0 in conjunction with the relationship $\sigma_b' = \sigma_0(1 - \Sigma_i \rho_i^2)$ produce a negative value of $\sigma_b' = -0.112$ that falls within the range of (negative) values determined by the estimated uncertainty and best-fit value of σ_b' obtained by fitting the experimental data using model III.

V. CONCLUSION

We have experimentally measured, theoretically calculated, and analyzed photoionization cross sections of atomic

argon which contain up to three overlapping Fano resonances. The overlapping nature of the resonances presents a challenge for the analysis. One can find different parameter sets that fit the data extremely well and yet have very different values. In order to guide our initial estimates for a fit to the experimental data, we used the parameters computed with the configuration interaction Pauli-Fock approach with core polarization. Using the combination of experiment and theory in the fitting procedure, we were able to determine a physically meaningful set of parameters for the resonances. In this way, we find that the experimental data and theoretical model are in good agreement. It remains to be seen whether or not the experimental method could be modified to extract accurate parameters without any reliance on theory; for instance, measuring the same final states from additional initial states could further constrain the fitting parameters, eliminate the possibility of finding different local minima in the parameter space of the residual-error function, and enable extraction of physically meaningful parameters. From the experimental point of view one would need to measure the cross section starting from at least three different initial states in order to identify the unique set of physically accurate parameters for three overlapping final states. In the present case only two cross sections were measured. Nonetheless, we were able to extract a set of physically meaningful parameters by using theoretically calculated parameters as a guide for the fitting procedure. Determination of these parameters would have been very difficult without both the experimental and theoretical results. Therefore the reported values for the Fano parameters of the 11p' resonances represent a synergy between experiment and theory.

[1] H. Beutler, Z. Phys. **93**, 177 (1935).
[2] U. Fano, Phys. Rev. **124**, 1866 (1961).
[3] U. Fano and J. W. Cooper, Phys. Rev. **137**, A1364 (1965).
[4] U. Fano and J. W. Cooper, Rev. Mod. Phys. **40**, 441 (1968). In this reference, σ_c denotes the same quantity as σ_0 in the present work.
[5] B. W. Shore, Rev. Mod. Phys. **39**, 439 (1967).
[6] B. W. Shore, J. Opt. Soc. Am. **57**, 881 (1967). In this reference, the symbol d denotes the trough depth, not the minimum value (trough depth multiplied by -1) of the profile function

as in the present work.
[7] B. W. Shore, Phys. Rev. **171**, 43 (1968).
[8] M. Aymar, O. Robaux, and C. Thomas, J. Phys. B **14**, 4255 (1981).
[9] M. J. Seaton, Rep. Prog. Phys. **46**, 167 (1983).
[10] U. Fano and A. R. P. Rau, *Atomic Collisions and Spectra* (Academic Press, Orlando, FL, 1986).
[11] K. Ueda, J. Opt. Soc. Am. B **4**, 424 (1987).
[12] A. L'Huillier, X. Tang, and P. Lambropoulos, Phys. Rev. A **39**, 1112 (1989).

[13] W. R. Johnson, K. T. Cheng, K.-N. Huang, and M. LeDourneuf, Phys. Rev. A **22**, 989 (1980).

[14] R. P. Wood, C. H. Greene, and D. Armstrong, Phys. Rev. A **47**, 229 (1993).

[15] J. Berkowitz, *Photoabsorption, Photoionization and Photoelectron Spectroscopy* (Academic Press, New York, 1979).

[16] K. D. Bonin, T. J. McIlrath, and K. Yoshino, J. Opt. Soc. Am. B **2**, 1275 (1985).

[17] J. Berkowitz, Adv. Chem. Phys. **72**, 1 (1988).

[18] K. Maeda, K. Ueda, and K. Ito, J. Phys. B **26**, 1541 (1993).

[19] S. M. Koeckhoven, W. J. Buma, and C. A. de Lange, Phys. Rev. A **49**, 3322 (1994).

[20] S. M. Koeckhoven, W. J. Buma, and C. A. de Lange, Phys. Rev. A **51**, 1097 (1995).

[21] M. Gisselbrecht, A. Marquette, and M. Meyer, J. Phys. B **31**, L977 (1998).

[22] I. D. Petrov, V. L. Sukhorukov, T. Peters, O. Zehnder, H. J. Wörner, F. Merkt, and H. Hotop, J. Phys. B **39**, 3159 (2006).

[23] I. D. Petrov, T. Peters, T. Halfmann, S. Aloise, P. O'Keeffe, M. Meyer, V. L. Sukhorukov, and H. Hotop, Eur. Phys. J. D **40**, 181 (2006).

[24] R. F. Stebbings, F. B. Dunning, and R. D. Rundel, in *Atomic Physics*, edited by G. Putlitz, E. W. Weber, and A. Winnacker (Plenum Press, New York, 1975), Vol. 4, pp. 713–730.

[25] H. Hotop, D. Klar, and S. Schohl, in *Proceedings of the 6th International Symposium on Resonance Ionization Spectroscopy (RIS-92)*, edited by C. M. Miller and J. E. Parks (IOP, Bristol, 1992) [Inst. Phys. Conf. Ser. **128**, 45 (1992)].

[26] D. Klar, K. Harth, J. Ganz, T. Kraft, M.-W. Ruf, H. Hotop, V. Tsemekhman, K. Tsemekhman, and M. Y. Amusia, Z. Phys. D **23**, 101 (1992).

[27] D. Klar, K. Ueda, J. Ganz, K. Harth, W. Bussert, S. Baier, J. M. Weber, M.-W. Ruf, and H. Hotop, J. Phys. B **27**, 4897 (1994).

[28] J. Bömmels, J. M. Weber, A. Gopalan, N. Herschbach, E. Leber, A. Schramm, K. Ueda, M.-W. Ruf, and H. Hotop, J. Phys. B **32**, 2399 (1999).

[29] D. Klar, M. Aslam, M. A. Baig, K. Ueda, M.-W. Ruf, and H. Hotop, J. Phys. B **34**, 1549 (2001).

[30] M. Hanif, M. Aslam, R. Ali, S. A. Bhatti, M. A. Baig, D. Klar, M.-W. Ruf, I. D. Petrov, V. L. Sukhorukov, and H. Hotop, J. Phys. B **37**, 1987 (2004).

[31] T. Peters, T. Halfmann, U. Even, A. Wünnenberg, I. D. Petrov, V. L. Sukhorukov, and H. Hotop, J. Phys. B **38**, S51 (2005).

[32] M. A. Baig, M. Hanif, M. Aslam, and S. A. Bhatti, J. Phys. B **39**, 4221 (2006).

[33] I. D. Petrov, V. L. Sukhorukov, and H. Hotop, J. Phys. B **35**, 323 (2002).

[34] I. D. Petrov, V. L. Sukhorukov, and H. Hotop, J. Phys. B **36**, 119 (2003).

[35] R. F. Stebbings and F. B. Dunning, Phys. Rev. A **8**, 665 (1973).

[36] F. B. Dunning and R. F. Stebbings, Phys. Rev. A **9**, 2378 (1974).

[37] A. Mühlpfordt and U. Even, J. Chem. Phys. **103**, 4427 (1995).

[38] A. F. Starace, *Theory of Atomic Photoionization*, Vol. 31 of Handbuch der Physik (Springer, Berlin, 1982), ISBN 3–540–11313–4.

[39] S. L. Sorensen, T. Åberg, J. Tulkki, E. Rachlew-Kallne, G. Sundstrom, and M. Kirm, Phys. Rev. A **50**, 1218 (1994).

[40] D. L. Ederer, Phys. Rev. A **4**, 2263 (1971); **14**, 1936(E) (1976).

[41] I. D. Petrov, V. L. Sukhorukov, and H. Hotop, J. Phys. B **41**, 065205 (2008).

[42] I. D. Petrov, V. L. Sukhorukov, and H. Hotop, J. Phys. B **32**, 973 (1999).

[43] I. D. Petrov, V. L. Sukhorukov, E. Leber, and H. Hotop, Eur. Phys. J. D **10**, 53 (2000).

[44] L. Minnhagen, J. Opt. Soc. Am. **63**, 1185 (1973).

[45] I. Velchev, W. Hogervorst, and W. Ubachs, J. Phys. B **32**, L511 (1999).

[46] S. Basu and J. L. Knee, J. Chem. Phys. **120**, 5631 (2004).

[47] W. H. Press, B. P. Flannery, S. A. Teukolsky, and W. T. Vetterling, *Numerical Recipes in Pascal* (Cambridge University Press, Cambridge, England, 1989).